Supporting Information

A "MOFs plus MOFs" strategy toward Co-Mo_2N tubes for efficient electrocatalytic overall water splitting

Xia Shi, Aiping Wu, Haijing Yan, Lin Zhang, Chungui Tian*, Lei Wang and Honggang Fu*

Key Laboratory of Functional Inorganic Material Chemistry, Ministry of Education, Heilongjiang University, Harbin 150080, China

E-mail: fuhg@vip.sina.com; fuhg@hlju.edu.cn; chunguitianhq@163.com

Contents

19 **Figure S19.** Cyclic voltammograms (CVs) in the region of 0.85 V-0.185 V with the different rates for **(a)** Mo-MOFs-T5; **(c)** ZIF-67-T5; **(e)** S-2-T5; **(g)** S-2-T4; **(i)** S-2-T6; **(k)** S-1-T5; **(m)** S-3-T5 in 1.0 M KOH. The capacitive current at 0.135 V as a function of scan rate for **(b)** Mo-MOFs-T5; **(d)** ZIF-67-T5; **(f)** S-2-T5; **(h)** S-2-T4; **(j)** S-2-T6; **(l)** S-1-T5; **(n)** S-3-T5, respectively ($\Delta j_0 = j_a - j_c$).

20 **Figure S20.** The cathodic (black open circle) and anodic (red open square) charging currents measured at 0.135V vs SCE plotted as a function of scan rate. (HER)

21 **Figure S21.** The cathodic (black open circle) and anodic (red open square) charging currents measured at 1.215V vs SCE plotted as a function of scan rate. (OER)

22 **Figure S22. (a)** CVs of S-2-T5, Mo-MOFs-T5 and ZIF-67-T5 in 1 M PBS (pH = 6.67) with a scan rate of 50 mV s^{-1}. **(b)** Calculated TOF for S-2-T5, Mo-MOFs-T5 and ZIF-67-T5 in 1 M KOH.

23 **Figure S23.** The Faradiac efficiency of (a) HER and (b) OER of S-2-T5.

24 **Figure S24.** The work function drawings of **(a)** S-2-T5; **(b)** Mo-MOFs-T5**; (c)** ZIF-67-T5; **(d)** Pt black. The WF values of the S-2-T5, Mo-MOFs-T5, ZIF-67-T5 and Pt black are about 5.56 eV, 5.37 eV, 5.49 eV and 5.60 eV, respectively.

25 **Figure S25. (a)** Polarization curves, **(b)** Tafel plots of the S-2-T4, S-2-T5 and S-2-T6 at 1.0 M KOH, respectively.

26 **Figure S26. (a)** Polarization curves. **(b)** Tafel plots of the S-1-T5, S-2-T5 and S-3-T5 at 1.0 M KOH, respectively.

27 **Figure S27.** (a) Polarization curves and (b) Tafel plots of S-2-T5 and Co+Mo_2N in 1 M KOH for the HER at a scan rate of 5 mV s^{-1}. (c) Polarization curves and (d) Tafel plots of S-2-T5 and Co+Mo_2N in 1 M KOH for the OER at a scan rate of 5 mV s^{-1}. (e) Linear sweeping voltammetry curve of S-2-T5 as OER and HER bifunctional catalyst in 1.0 M KOH for overall water splitting, and Co+Mo_2N‖Co+Mo_2N for overall water splitting.

28 **Figure S28.** Cyclic voltammograms (CVs) in the region of 1.164 V-1.264 V with the different rates for **(a)** Mo-MOFs-T5; **(c)** ZIF-67-T5; **(e)** S-2-T5; **(g)** S-2-T4; **(i)** S-2-T6; **(k)** S-1-T5; **(m)** S-3-T5 in 1.0 M KOH. The capacitive current at 0.135 V as a function of scan rate for **(b)** Mo-MOFs-T5; **(d)** ZIF-67-T5; **(f)** S-2-T5; **(h)** S-2-T4; **(j)** S-2-T6; **(l)** S-1-T5; **(n)** S-3-T5, respectively ($\Delta j_0 = j_a - j_c$).

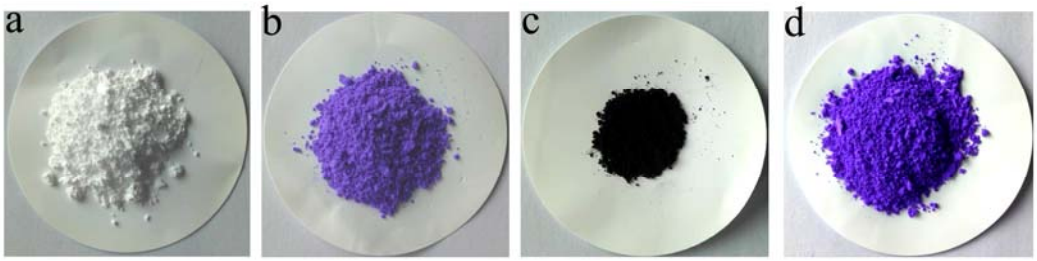

Figure S1. The optical photographs of products including Mo-MOFs (a); ZIF-67/Mo-MOFs-2 (b); S-2-T5 (c) and ZIF-67 (d), respectively.

The formation of samples from different stage can be reflected by colour change of solids. Typically, the Mo-MOFs show white color. After growth of ZIF-67, the color is changed to uniform purple close to that of ZIF-67, implying the formation of ZIF-67 on Mo-MOFs. The black color after nitridation is indicative to form Co-Mo_2N hybrids. The ZIF-67 shows an expected purple.

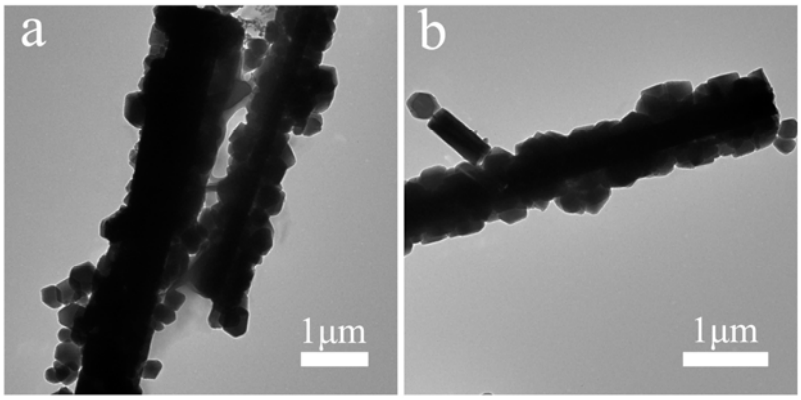

Figure S2. The low-magnification of TEM images of ZIF-67/Mo-MOFs-2 precursor shown in different areas of TEM grid. The results indicate that the ZIF-67 is growth on 1-D Mo-MOFs.

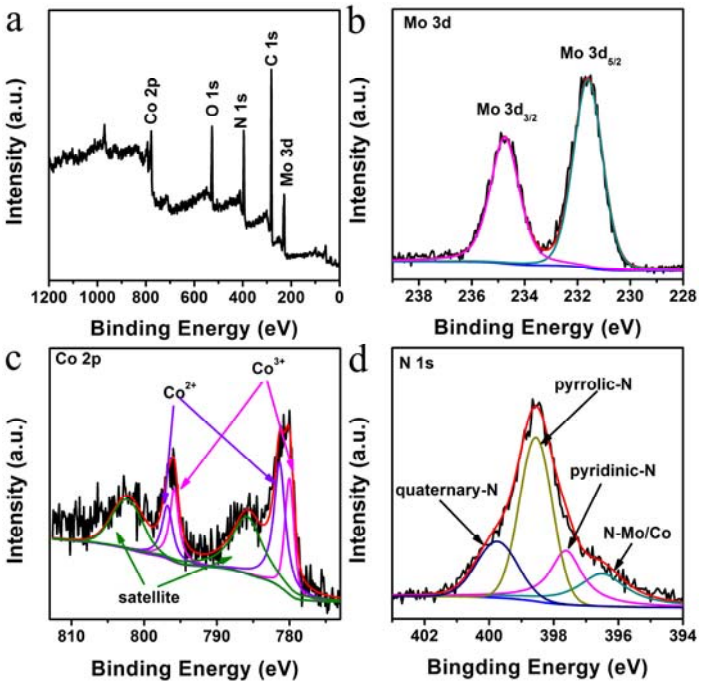

Figure S3. (a) The XPS survey spectrum and the high-resolution XPS spectra of **(b)** Mo 3d, **(c)** Co 2p and **(d)** N 1s for ZIF-67/Mo-MOFs-2 precursor.

Figure S3 shows XPS spectra of ZIF-67/Mo-MOFs-2. Figure S3a shows a wide-scan spectrum of the Mo-MOFs-T5. The sharp peaks at 284.0 eV, 395.5 eV, 528.0 eV, 228.9 eV and 778.0 eV are characteristic peaks of C 1s, N 1s, O 1s, Mo 3d and Co 2p, respectively. High resolution XPS spectra of Mo elements are shown in Figure S3b. The Mo 3d spectra can be fitted into two peaks. The peaks at the binding energies of 231.6 eV and 234.8 eV are attributed to Mo $3d_{5/2}$ and Mo $3d_{3/2}$ of Mo^{6+} in Mo-MOFs.

Figure S3c shows the high-resolution spectrum of the cobalt element. The spin-orbit splitting is approximately 15.8 eV, which indicates the co-existence of Co (II) and Co (III) in the material. The peaks at about 781.4 eV and 796.8 eV corresponding to Co $2p_{3/2}$ and Co $2p_{1/2}$ of Co^{2+} in ZIF-67, which are accompanied by a couple of satellite peaks located at 785.9 eV and 802.5 eV. The binding energies at about 780.0 eV and 795.9 eV are attributed to Co $2p_{3/2}$ and Co $2p_{1/2}$ of Co^{3+} in Co_2O_3. The above result illustrates the formation of ZIF-67.

As shown in Figure S3d, the high-resolution spectrum of N element shows four deconvoluted peaks at 396.5, 397.7, 398.6 and 399.8 eV. The peaks located at 399.8 eV, 398.6 eV and 397.7 eV can be assigned to quaternary N, pyrrolic N and pyridinic N, respectively. Besides, the peak at 396.5 eV is the typical binding energy of N to Mo/Co. These results show the formation of ZIF-67/Mo-MOFs-2 precursor.

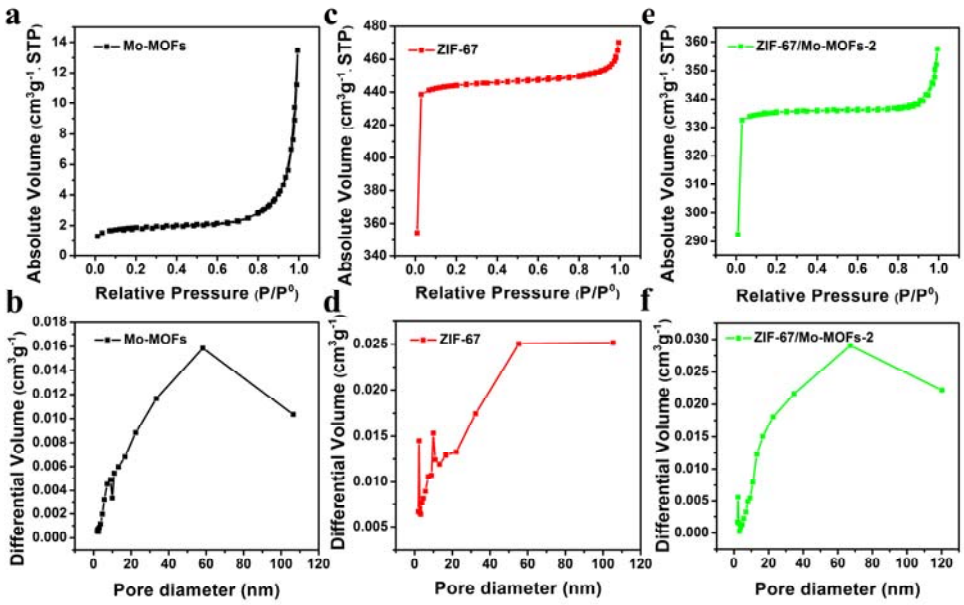

Figure S4. N_2 adsorption-desorption isotherms and pore size distribution patterns for Mo-MOFs **(a.b.)**; ZIF-67 **(c.d.)**; ZIF-67/Mo-MOFs-2 **(e.f.)**;

N_2 adsorption-desorption isotherms test results show that the Brunauer-Emmett-Teller (BET) specific surface area of ZIF-67/Mo-MOFs-2 is about 1143 $m^2\ g^{-1}$. The Mo-MOFs and ZIF-67 have shown S_{BET} of 6 $m^2\ g^{-1}$ and 1512 $m^2\ g^{-1}$, respectively (Figure S4, Supporting Information). The high specific surface area of ZIF-67 is relative with its plentiful micro-pores. The specific surface area of ZIF-67/Mo-MOFs-2 is between ZIF-67 and Mo-MOFs, which also implies a successful combination of ZIF-67 and Mo-MOFs

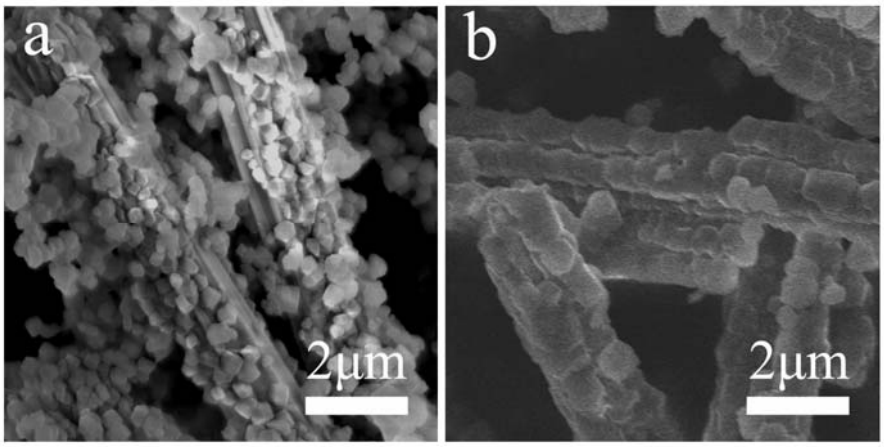

Figure S5. SEM images of the synthesized (a) ZIF-67/Mo-MOFs-1; (b) ZIF-67/Mo-MOFs-3.

The SEM test shows that the coverage and size of ZIF-67 can be increased with decreasing the ratio of Co/Mo source. However, the excessive increase of Co/Mo ratio can result in the formation of a large amount of free ZIF-67 that not loaded onto Mo-MOFs (Figure S5a). A suitable ratio of Co and Mo source can give hybrid with high coverage of ZIF-67 on Mo-MOFs. The tunable Co/Mo ratio is very important for their application.

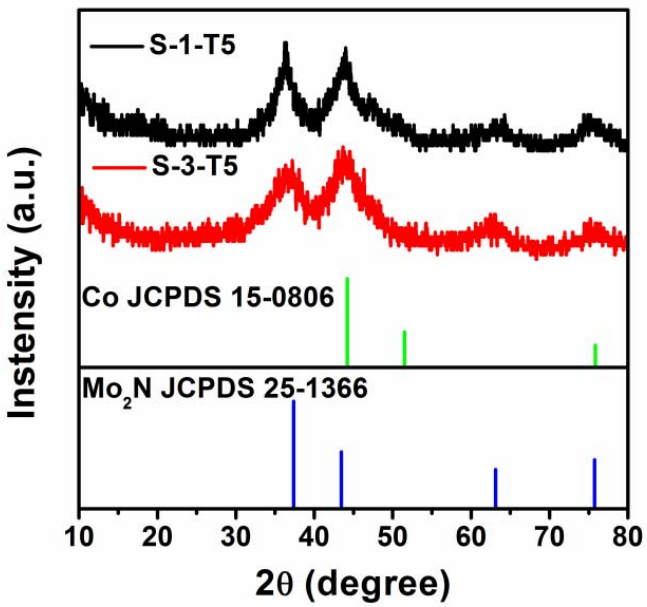

Figure S6. XRD patterns of S-1-T5 and S-3-T5.

The samples contained different ratio of ZIF-67 and Mo-MOFs, that is, ZIF-67/Mo-MOFs-1 (S-1-T5) and ZIF-67/Mo-MOFs-3 (S-3-T5) were calcinated at 500 ^{0}C under NH_3 to given S-1-T5 and S-3-T5. The samples exhibit XRD diffraction peaks at 2θ = 36.35°, 43.97°, 63.18° and 75.74°, indexing to the Mo_2N (JCPDS No. 25-1366) and Co (JCPDS No. 15-0806). The XRD tests indicated that the diffraction peak located at 43.97° (Co metal) degree increase with the increase ratio of ZIF-67/Mo-MOFs in the precursor. There are no diffractions corresponding to additional Co species (CoO_x or CoN_x) besides the diffraction of metal Co. The results indicated that we can prepare the formation of Co-Mo_2N with tunable ratio.

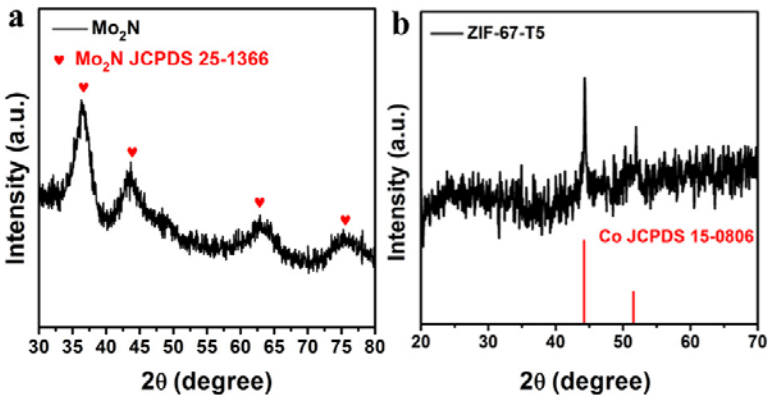

Figure S7. XRD patterns of **(a)** Mo-MOFs-T5; **(b)** ZIF-67-T5.

Figure S7 shows the XRD patterns of Mo-MOFs-T5 and ZIF-67-T5. The characteristic peaks of the Mo-MOFs-T5 were found to match the characteristic peaks of Mo_2N (JCPDS No. 25-1366). The XRD results of ZIF-67-T5 indicate the formation of metal Co (JCPDS No. 15-0806).

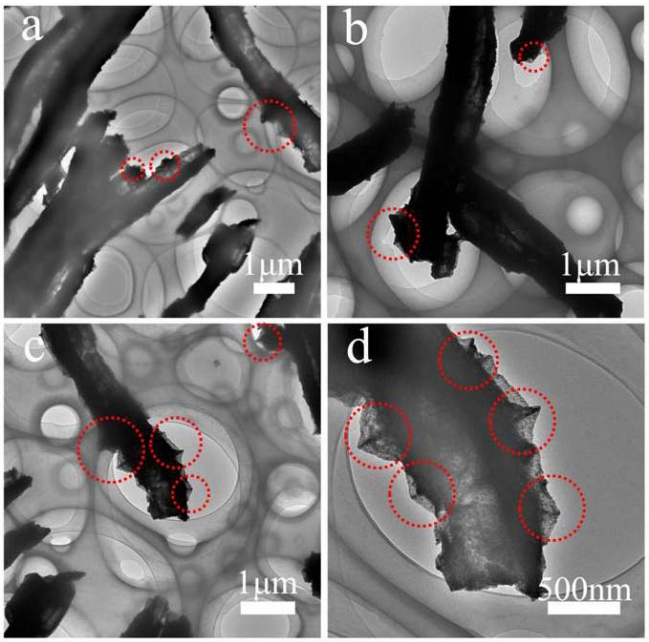

Figure S8. TEM images of the Co-Mo_2N. The marked areas show obviousy the growth of Co on 1-D Mo^2N.

Figures S8 shows that the Co-Mo_2N from different area of TEM grid. We can see the formation of hollow tubes in large areas. In addition, we can observe the polyhedron derived from ZIF-67 in high-magnification TEM images (red ring position). The polyhedrons are not obvious in some areas, which should be relative with the unsuitable place for TEM observe or small size of ZIF-67 precursor.

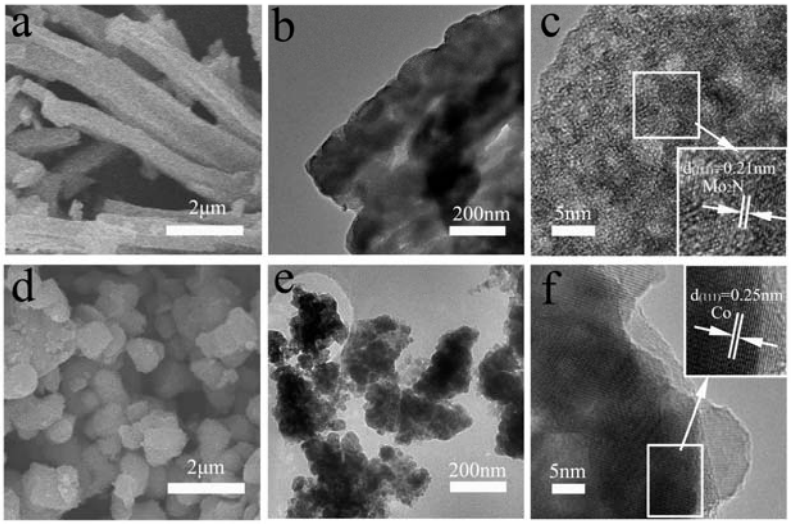

Figure S9. SEM, TEM, HRTEM images **(a-c)** of the Mo-MOFs-T5 and **(d-f)** of ZIF-67-T5.

Figure S9 shows SEM and TEM images of Mo-MOFs-T5 and ZIF-67-T5. As can be seen from Figure S9a-b, the Mo-MOFs-T5 have show 1-D structure with rough surface, which is different with the original Mo-MOFs with smooth surface. The change implies the formation of Mo_2N. The TEM image (Figure S9c) shows the lattice fringe of 0.21 nm associated with (111) crystal plane of Mo_2N (JCPDS No.25-1366). The HRTEM have also shown the presence of some pore on Mo-MOFs-T5 surface, which is different with the coarse surface on Co-Mo_2N. The material derived from ZIF-67 shows irregular morphology, which should due to that the high temperature calcination under NH_3 makes the collapsing of the sample. The high-resolution TEM of ZIF-67-T5 shows a lattice spacing of 0.25 nm, corresponding to (111) crystal plane of metallic Co (JCPDS No.15-0806).

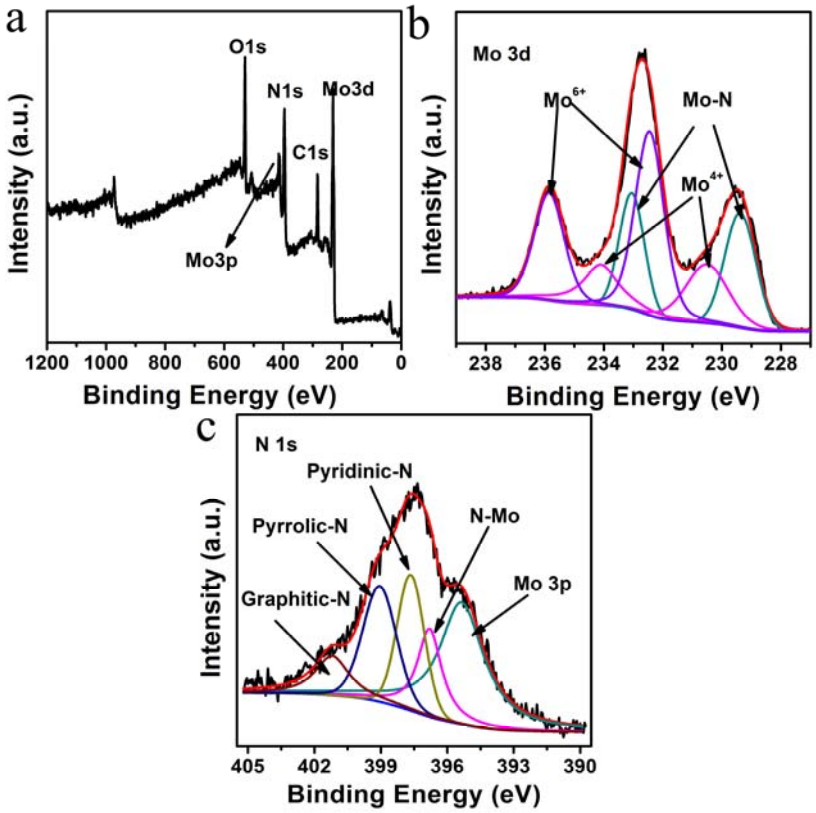

Figure S10. The XPS survey spectrum **(a)** and the high-resolution XPS spectra of Mo 3d **(b)** and N 1s **(c)** in Mo-MOFs-T5.

Figure S10a shows a wide-scan spectrum of the Mo-MOFs-T5. The sharp peaks at 285.3 eV, 395.5 eV, 528.3 eV, 228.9 eV and 412.5 eV are indexed as the characteristic peaks of C 1s, N 1s, O 1s, Mo 3d and Mo 3p, respectively. The high resolution XPS spectra of the Mo element (Figure S10b) shows that the Mo 3d spectra can be fitted into six peaks. The peaks at the binding energies of 230.5 eV and 234.2 eV are classified as Mo $3d_{5/2}$ and Mo $3d_{3/2}$ of Mo^{4+} in MoO_2 and the peaks at the binding energies of 232.5 eV and 235.9 eV are attributed to Mo $3d_{5/2}$ and Mo $3d_{3/2}$ of Mo^{6+} in MoO_3. The binding peaks at 229.4 eV and 233.1 eV are defined as the binding energies of the Mo-N bond in Mo_2N, which shows the formation of nitride. The XPS results of Mo-MOFs-T5 are consistent with that of Mo_2N reported. As shown in Figure S10c, the high-resolution spectrum of the N element can be deconvoluted into five peaks at 395.4, 396.8, 397.6, 399.1 and 401.2 eV. Firstly, 401.2 eV, 399.1 eV and 397.6 eV can be assigned to graphitic N, pyrrolic N and pyridinic N, respectively. The peak at 396.8 eV is the typical binding energies of N combined with Mo, which shows the formation of nitrides. The above data further indicate the formation of Mo_2N.

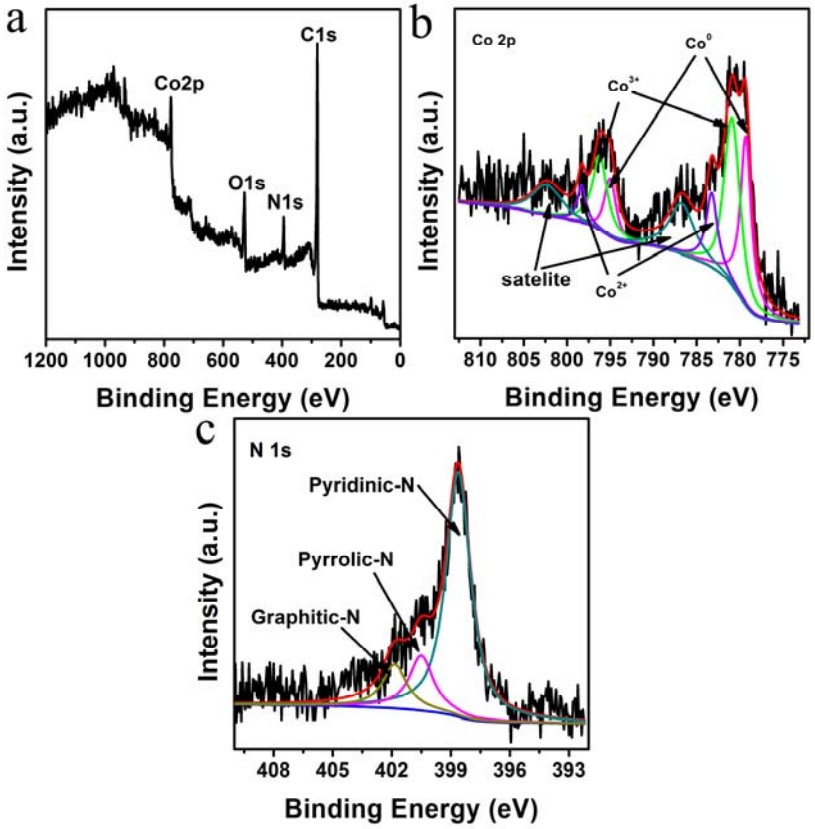

Figure S11. (a) The XPS survey spectrum and the high-resolution XPS spectra (b) of Co 2p and **(c)** N 1s in ZIF-67-T5.

Figure S11a shows a wide-scan spectrum of the ZIF-67-T5. The sharp peaks at 279.7 eV, 392.6 eV, 528.3 eV and 776.9 eV are indexed as the characteristic peaks of C 1s, N 1s, O 1s and Co 2p, respectively. The above information suggesting the existence of carbon (C), nitrogen (N), oxygen (O) and cobalt (Co) elements on the surfaces of ZIF-67-T5.

As shown in Figure S11b, the high-resolution spectrum of Co element shows the spin-orbit splitting about 15.8 eV, which indicates the co-existence of the Co (II) and Co (III). The peaks at about 783.2 eV and 798.3 eV correspond to Co $2p_{3/2}$ and Co $2p_{1/2}$ of Co^{2+} in CoO, respectively, which are accompanied by a couple of satellite peaks located at 786.7 eV and 802.3 eV. The binding energies at about 780.9 eV and 796.2 eV are attributed to Co $2p_{3/2}$ and Co $2p_{1/2}$ of Co^{3+} in Co_2O_3. The peaks located at 779.3 eV and 795.0 eV in Co 2p spectrum is assigned to Co^0 $2p_{3/2}$ and Co^0 $2p_{1/2}$, respectively. The presence of oxides should be ascribed to easy oxidation of metal Co under air. In the high-resolution spectrum of N element (Figure S11c), we can see three peaks at 401.9, 400.5 and 398.6 eV, which are assigned to graphitic N, pyrrolic N and pyridinic N, respectively.

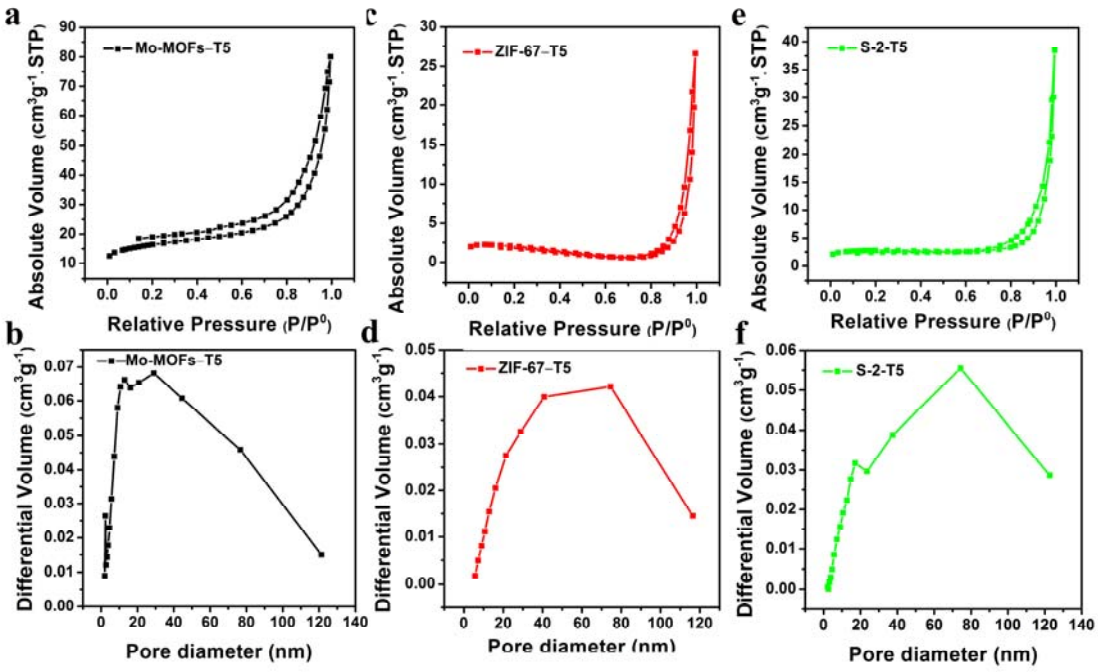

Figure S12. N_2 adsorption-desorption isotherms and pore size distribution patterns for **(a, b)** Mo-MOFs-T5, **(c, d)** ZIF-67-T5, **(e, f)** S-2-T5.

The nitrogen adsorption-desorption isotherms test indicated that S_{BET} value of ZIF-67-T5 is about 6 m^2 g^{-1}. The dramatic reduction in the specific surface area should be due to the collapse of the well-defined microporous structure of ZIF-67 caused by the nitrogenization. The Mo-MOFs-T5 has rod-like structure with a rough surface. Its specific surface area has slight increase compared to the precursor. The S-2-T5 (9 m^2 g^{-1}) has shown a lower specific surface area than Mo-MOF-T5 (57 m^2 g^{-1}). The decrease should be ascribed to the coverage of Co derived from ZIF-67 polyhedron on Mo_2N, which is an indicative for the formation of Co-Mo_2N hybrid.

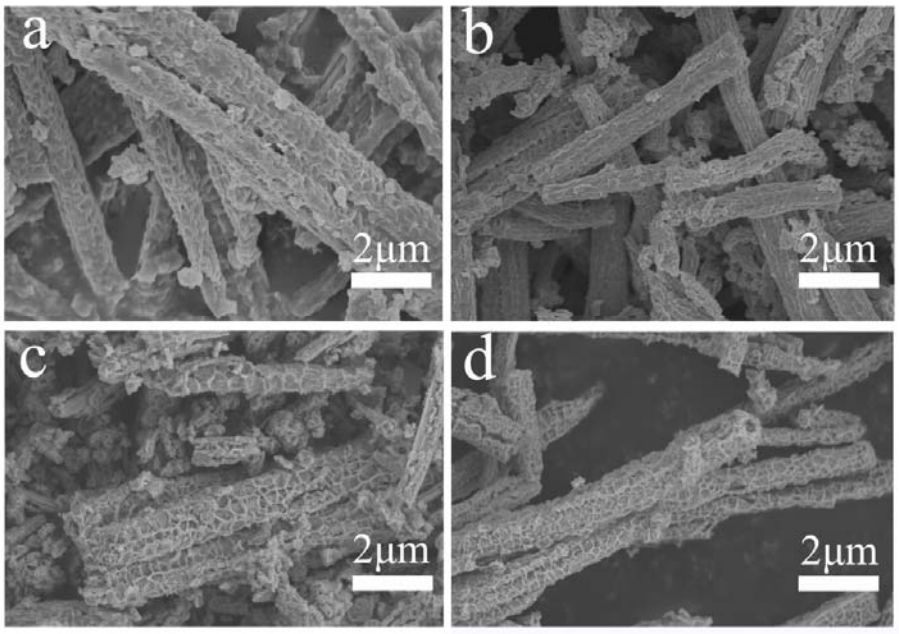

Figure S13. SEM images of the S-2-T4 **(a)**; S-2-T6 **(b)**; S-1-T5 **(c)**; S-3-T5 **(d)**.

The SEM images of different samples are shown in Figure S13. We can see all control samples, including S-2-T4 (a), S-2-T6 (b), S-1-T5 (c) and S-3-T5 (d), show the 1-D rod-like structure.

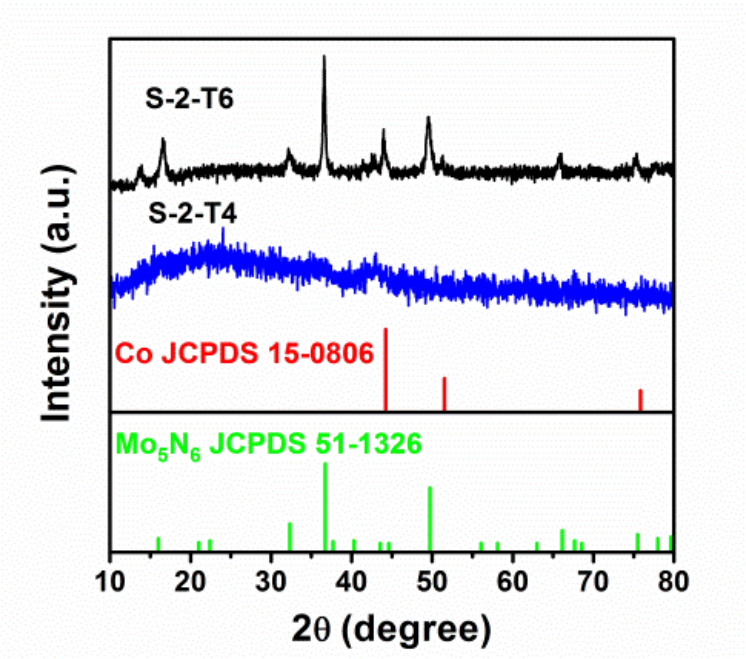

Figure S14. XRD patterns of S-2-T4 and S-2-T6.

Figure S14 shows the XRD patterns of S-2-T4 and S-2-T6 from the calcination of ZIF-67/Mo-MOF-2 at 400 and 600 ^{0}C, respectively. The XRD pattern of S-2-T4 shows very low diffraction peaks of Co metal, and there are no obvious peaks about Mo_2N phase. In the case of calcination at 600 ^{0}C, the crystallization phase of material are composed of Co and Mo_5N_6. The intensive peaks imply the good crystallinity and larger grain sizes. The results show the important effect of calcination temperature on the structure.

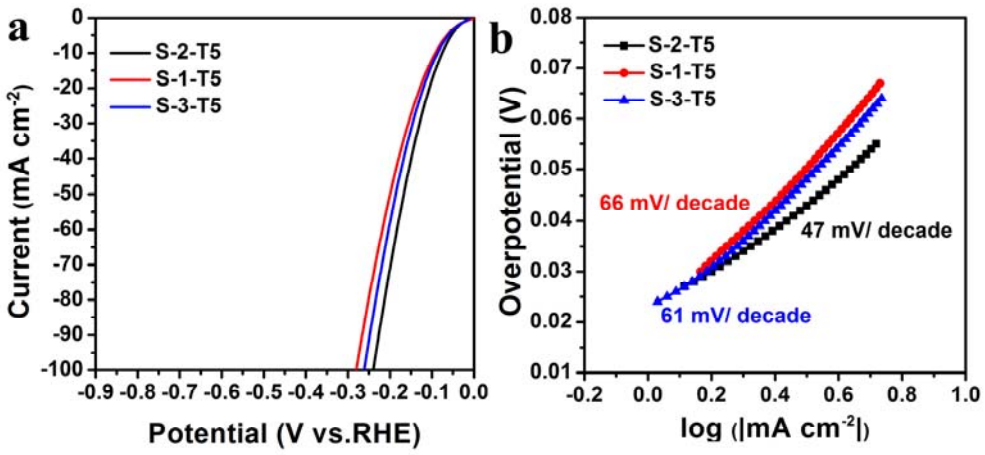

Figure S15. (a) Polarization curves, **(b)** Tafel plots of the S-1-T5, S-2-T5 and S-3-T5 at 1.0 M KOH, respectively.

The comparison shows that the HER performance of S-2-T5 is better than that of S-1-T5 and S-3-T5. In the case of low Co/Mo ratio, the coverage of Co on Mo_2N is very low, resulting in little contacted interface of Co and Mo_2N (Generally speaking, the interface of heterojunction is more active than other sites), and consequently, the lower activity for HER. The high ratio of Co and Mo can make the formation of free Co species derived from free ZIF-67.

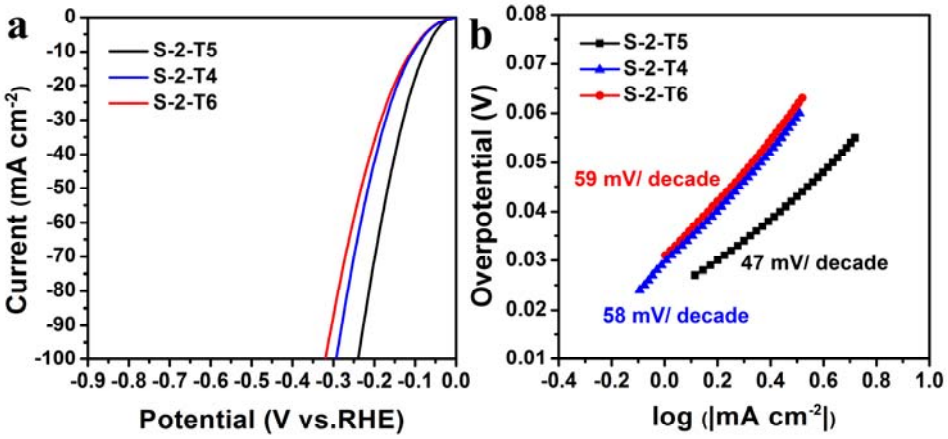

Figure S16. (a) Polarization curves, **(b)** Tafel plots of the S-2-T4, S-2-T5 and S-2-T6 at 1.0 M KOH, respectively.

The comparison shows that the HER performance of S-2-T5 is better than that of S-2-T4 and S-2-T6. The calcination at low temperature is not favourable for the formation of Co and Mo_2N, while the high-treatment temperature can result in the excessive growth of sample. Both of them are not conductive to improve the catalytic activity. It can be concluded that the appropriate crystallinity and ratio of Co/Mo are great importance for the effective HER.

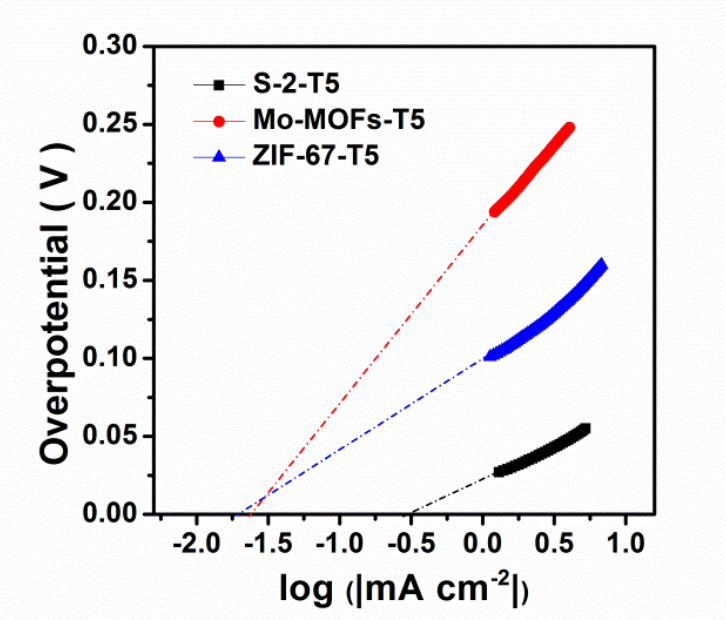

Figure S17. Calculation of exchange current density of S-2-T5, Mo-MOFs-T5 and ZIF-67-T5.

The exchange current density (j_0) was calculated by using extrapolation method (Figure S17). At the overpotential of 0, the log [j] values for S-2-T5, Mo-MOFs-T5 and ZIF-67-T5 are -0.52, -1.60 and -1.73, respectively. So, the j_0 for S-2-T5 is about 0.302 mA cm^{-2}, much higher than Mo-MOFs-T5 (0.025 mA cm^{-2}) and ZIF-67-T5 (0.019 mA cm^{-2}).

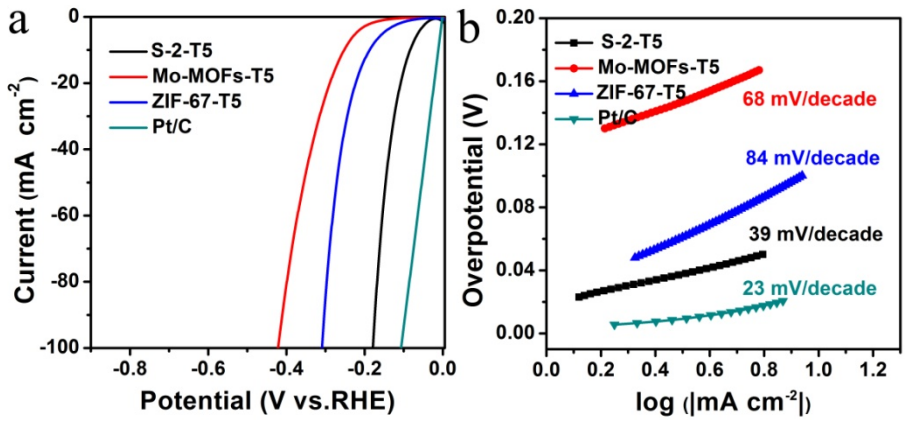

Figure S18. (a) Polarization curves and (b) Tafel plots of S-2-T5, Mo-MOF-T5, ZIF-67-T5 and Pt/C in 1 M KOH for the HER at a scan rate of 5 mV s^{-1}. (with IR compensation)

We further performed IR compensation tests on S-2-T5, Mo-MOF-T5, ZIF-67-T5 and Pt/C (Figure S18). The results show the Tafel slopes are about 39, 68, 84 and 23 mV dec^{-1} (1.0 M KOH) for S-2-T5, Mo-MOFs-T5, ZIF-67-T5 and Pt/C, respectively. And the S-2-T5 sample only requires a small overpotential of 73 mV to achieve the current densities of 10 mA cm^{-2} which is superior to Mo-MOFs-T5 (252 mV) and ZIF-67-T5 (186 mV) and the state-of-the-art Pt/C (17 mV).

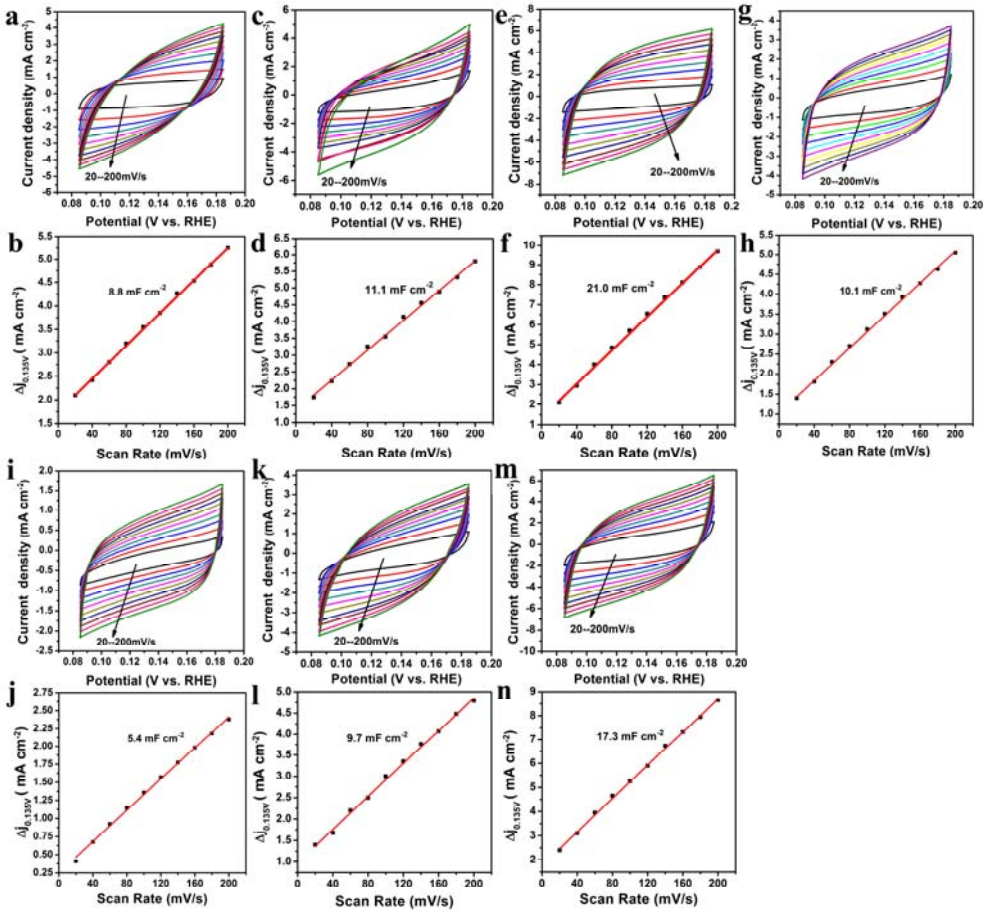

Figure S19. Cyclic voltammograms (CVs) in the region of 0.85 V-0.185 V with the different rates for **(a)** Mo-MOFs-T5; **(c)** ZIF-67-T5; **(e)** S-2-T5; **(g)** S-2-T4; **(i)** S-2-T6; **(k)** S-1-T5; **(m)** S-3-T5 in 1.0 M KOH. The capacitive current at 0.135 V as a function of scan rate for **(b)** Mo-MOFs-T5; **(d)** ZIF-67-T5; **(f)** S-2-T5; **(h)** S-2-T4; **(j)** S-2-T6; **(l)** S-1-T5; **(n)** S-3-T5, respectively ($\Delta j_0 = j_a - j_c$).

The capacitance of S-2-T5 calculated based on active surface area is about 21.0 mF cm^{-2}, much higher than ZIF-67-T5 (11.1 mF cm^{-2}), Mo-MOFs-T5 (8.8 mF cm^{-2}), S-2-T4 (10.1 mF cm^{-2}), S-2-T6 (5.4 mF cm^{-2}), S-1-T5 (9.7 mF cm^{-2}) and S-3-T5 (17.3 mF cm^{-2}).

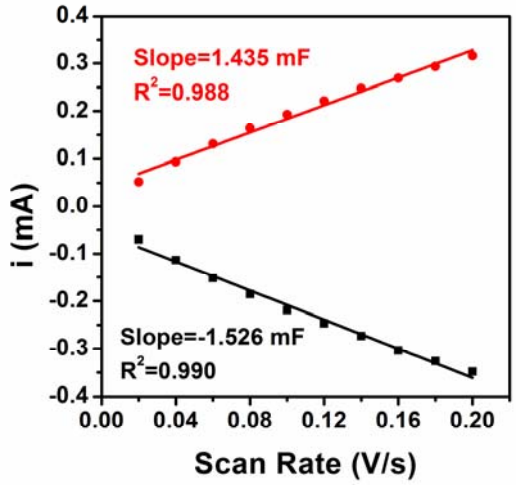

Figure S20. The cathodic (black open circle) and anodic (red open square) charging currents measured at 0.135V vs SCE plotted as a function of scan rate. (HER)

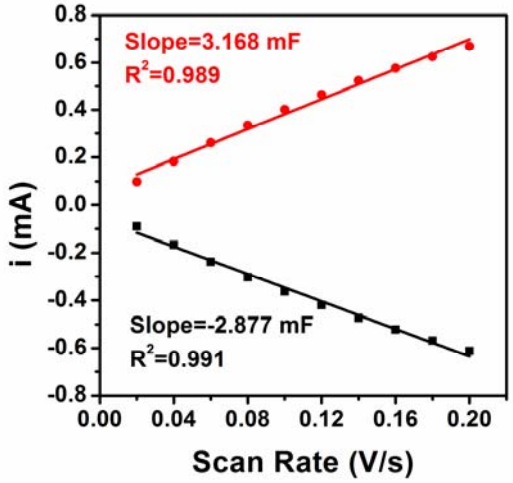

Figure S21. The cathodic (black open circle) and anodic (red open square) charging currents measured at 1.215V vs SCE plotted as a function of scan rate. (OER)

We have reviewed the literature on the relationship between the specific surface area of the material and the roughness factor.[1,2] By conducting the electrochemically active surface area test on the material, multiple CVs can then be performed at various scan rates for estimation of charging current (i_c). The relation between i_c, the scan rate (ν), and the double-layer capacitance (C_{dl}) is given in eq 1. Hence, the slope of i_c as a function of scan rate is a straight line and is equal to C_{dl}.

$$i_c = \nu C_{dl} \qquad (1)$$

The C_{dl} of the Co-Mo_2N hybrid HER and OER are 1.435 mF and 3.168 mF, respectively, which are converted to ECSA according to eq 2. A specific capacitance

(C_s) value C_s=0.040 mF cm^{-2} in 1.0 M KOH is adopted from previous reports, and hence ECSA of the HER and OER of the Co-Mo_2N hybrid were 35.9 mF and 79.2 mF, respectively.

$$ECSA = C_{dl}/C_s \quad (2)$$

Finally, the roughness factor (RF) is calculated on the basis of eq 3; given the geometric surface area (GSA) of working electrode (0.07065 cm^2), the RF of the HER and OER of the Co-Mo_2N hybrid were 508 and 1121 mF, respectively.

$$RF = ECSA/GSA \quad (3)$$

[1] C. C. L. McCrory, S. Jung, J. C. Peters and T. F. Jaramillo, J. Am. Chem. Soc., 2013, 135, 16977-16987.

[2] K. Akbar, J. H. Jeon, M. Kim, J. Jeong, Y. Yi and S.-H. Chun, ACS Sustainable Chem. Eng., 2018, 6, 7735-7742.

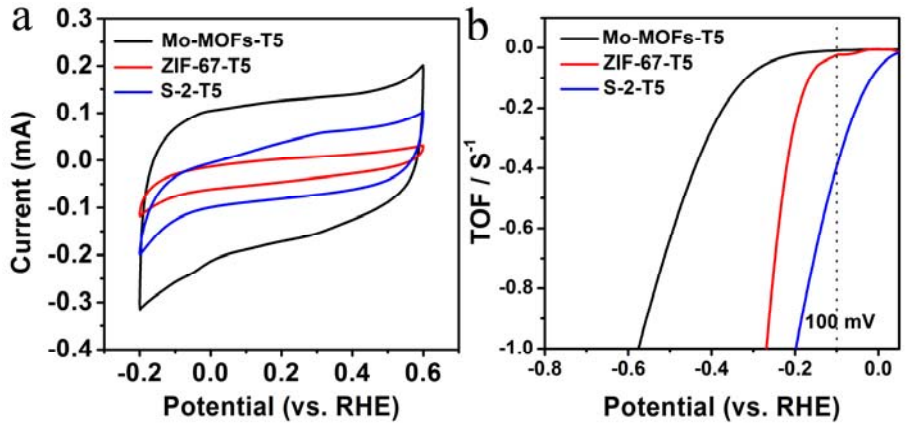

Figure S22. (a) CVs of S-2-T5, Mo-MOFs-T5 and ZIF-67-T5 in 1 M PBS (pH = 6.67) with a scan rate of 50 mV s^{-1}. **(b)** Calculated TOF for S-2-T5, Mo-MOFs-T5 and ZIF-67-T5 in 1 M KOH.

The turnover frequency (TOF) value is important parameter to evaluate the intrinsic activity of catalysts. For HER, the turnover frequency (TOF) is the number of H_2 molecules produced per second per active map. The number of active sites was examined by CV in a pH = 6.67 phosphate buffer with a scan rate of 50 mV s^{-1}. As shown in Figure S19, the S-2-T5 has highest TOF of 0.396 s^{-1} per site at overpotential of 100 mV, which is larger than that of 0.025 s^{-1} and 0.009 s^{-1} for ZIF-67-T5 and Mo-MOFs-T5, respectively.

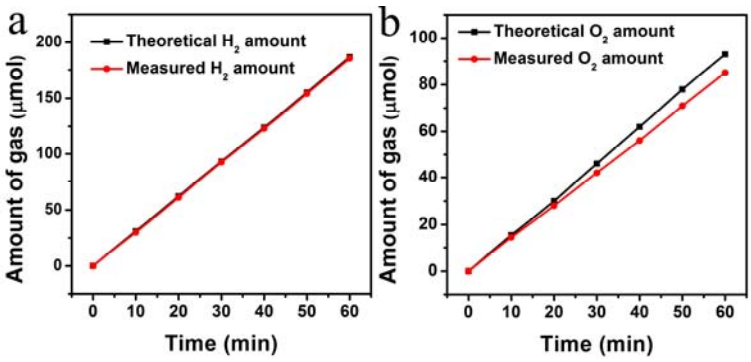

Figure S23. The Faradiac efficiency of (a) HER and (b) OER of S-2-T5.

The Faradiac efficiency of S-2-T5 for HER and OER is about 100% and 91% at 60 min of test.

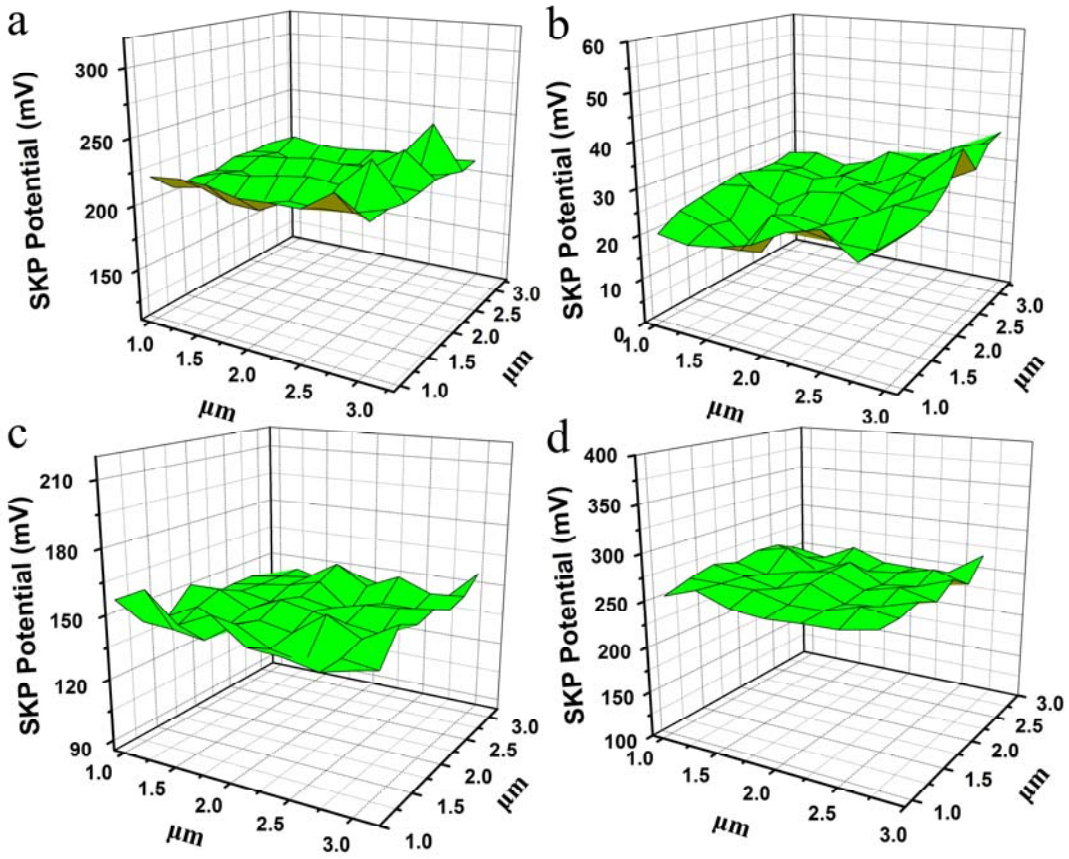

Figure S24. The work function drawings of **(a)** S-2-T5; **(b)** Mo-MOFs-T5**; (c)** ZIF-67-T5; **(d)** Pt black. The WF values of the S-2-T5, Mo-MOFs-T5, ZIF-67-T5 and Pt black are about 5.56 eV, 5.37 eV, 5.49 eV and 5.60 eV, respectively.

The work function (φ) of the material is calculated by the following formula:

$$\varphi_{Au} - \eta_{Au} /1000 = \varphi - \eta /1000$$

In which φ_{Au} is the work function of Au, $\eta_{Au} = -239.75$ eV. φ is the work function of material, η is derived from the work function test data.

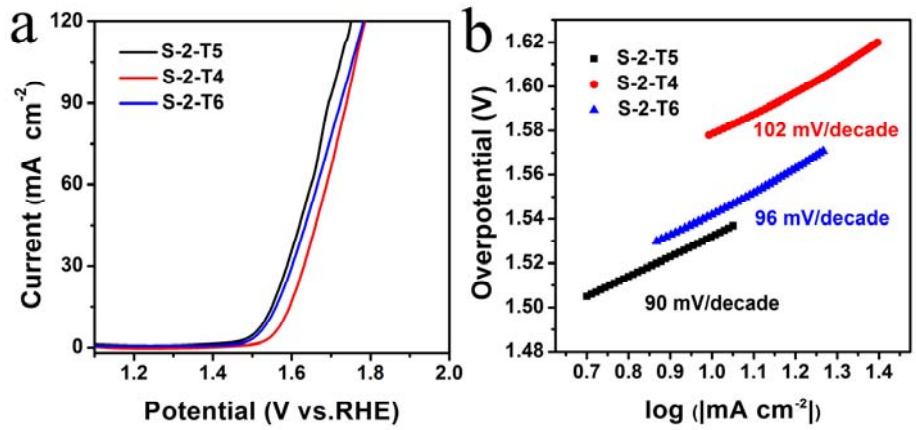

Figure S25. (a) Polarization curves, **(b)** Tafel plots of the S-2-T4, S-2-T5 and S-2-T6 at 1.0 M KOH, respectively.

The comparison shows that the OER performance of S-2-T5 is better than that of S-2-T4 and S-2-T6. The S-2-T5 affords overpotential of 302 mV at 10 mA cm^{-2}, which are much lower than S-2-T4 (348 mV) and S-2-T6 (312 mV) (Figure S25a). The Tafel slope of S-2-T5 is 90 mV dec^{-1}, which is also lower than S-2-T4 (102 mV dec^{-1}) and S-2-T6 (96 mV dec^{-1}) (Figure S25b).

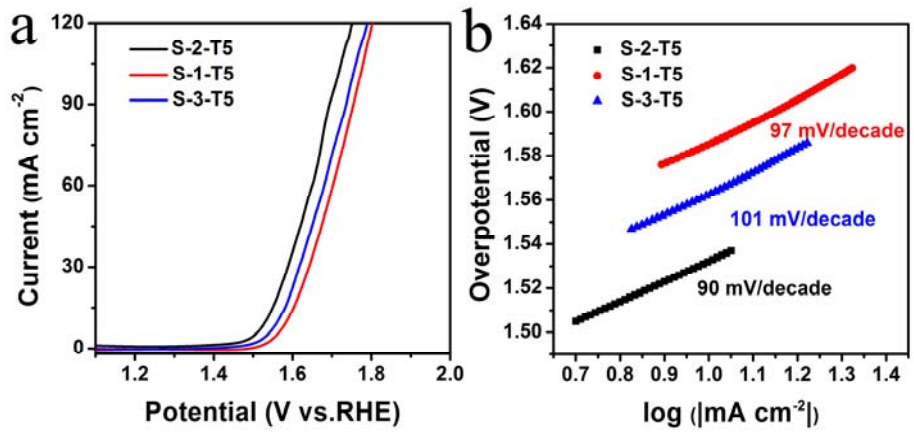

Figure S26. (a) Polarization curves. **(b)** Tafel plots of the S-1-T5, S-2-T5 and S-3-T5 at 1.0 M KOH, respectively.

The comparison shows that the OER performance of S-2-T5 is better than that of S-1-T5 and S-3-T5. The S-2-T5 affords overpotential of 302 mV at 10 mA cm^{-2}, which are much lower than S-1-T5 (356 mV) and S-3-T5 (333 mV) (Figure S26a). The Tafel slope of S-2-T5 is 90 mV dec^{-1}, which is also lower than S-1-T5 (97 mV dec^{-1}) and S-3-T5 (101 mV dec^{-1}) (Figure S26b).

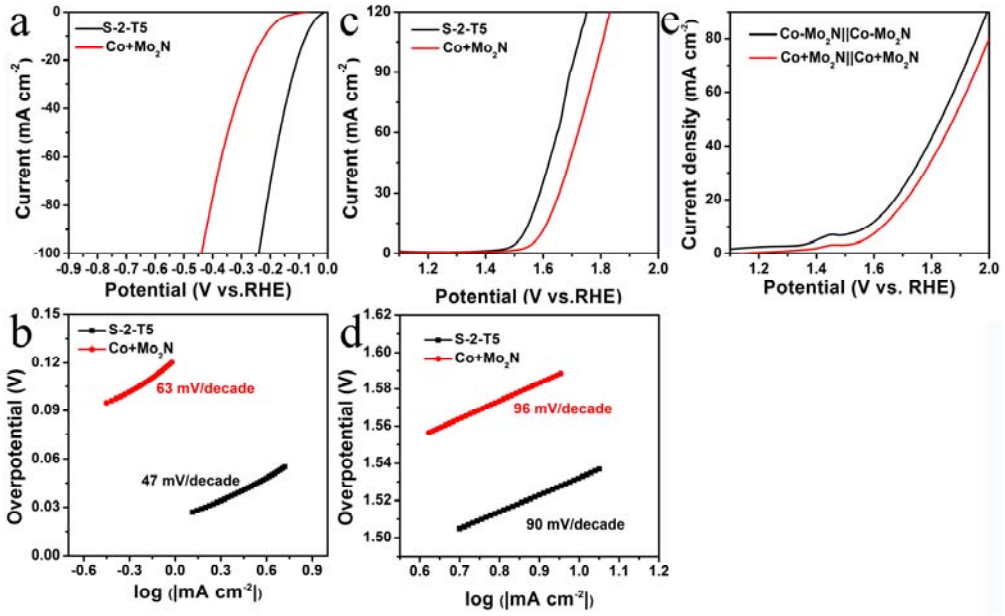

Figure S27. (a) Polarization curves and (b) Tafel plots of S-2-T5 and Co+Mo_2N in 1 M KOH for the HER at a scan rate of 5 mV s^{-1}. (c) Polarization curves and (d) Tafel plots of S-2-T5 and Co+Mo_2N in 1 M KOH for the OER at a scan rate of 5 mV s^{-1}. (e) Linear sweeping voltammetry curve of S-2-T5 as OER and HER bifunctional catalyst in 1.0 M KOH for overall water splitting, and Co+Mo_2N‖Co+Mo_2N for overall water splitting.

As control, the catalyst from physical mixing of Mo_2N and Co is prepared and used as catalyst for HER and OER reaction. Figure S27a and S27b show the Polarization curves and Tafel plots of Co + Mo_2N in 1 M KOH for the HER. For clarification, the curves corresponding to S-2-T5 are also added. The comparison shows that the HER performance of S-2-T5 is better than that of Co+Mo_2N. The S-2-T5 affords overpotential of 76 mV at 10 mA cm^{-2}, which is much lower than Co+Mo_2N (356 mV) (Figure S27a). The Tafel slope of S-2-T5 is 47 mV dec^{-1}, which is also lower than Co+Mo_2N (63 mV dec^{-1}) (Figure S27b). At the same time, the OER performance of S-2-T5 is better than that of Co+Mo_2N (Figure S27c). The S-2-T5 affords overpotential of 302 mV at 10 mA cm^{-2}, which is much lower than Co+Mo_2N (373 mV) (Figure S27c). The Tafel slope of S-2-T5 is 90 mV dec^{-1}, which is also lower than Co+Mo_2N (96 mV dec^{-1}) (Figure S27d). Finally, the S-2-T5 affords overpotential of 346 mV at 10 mA cm^{-2} for the overall water splitting, which is much lower than Co+Mo_2N (399 mV) (Figure S27e).

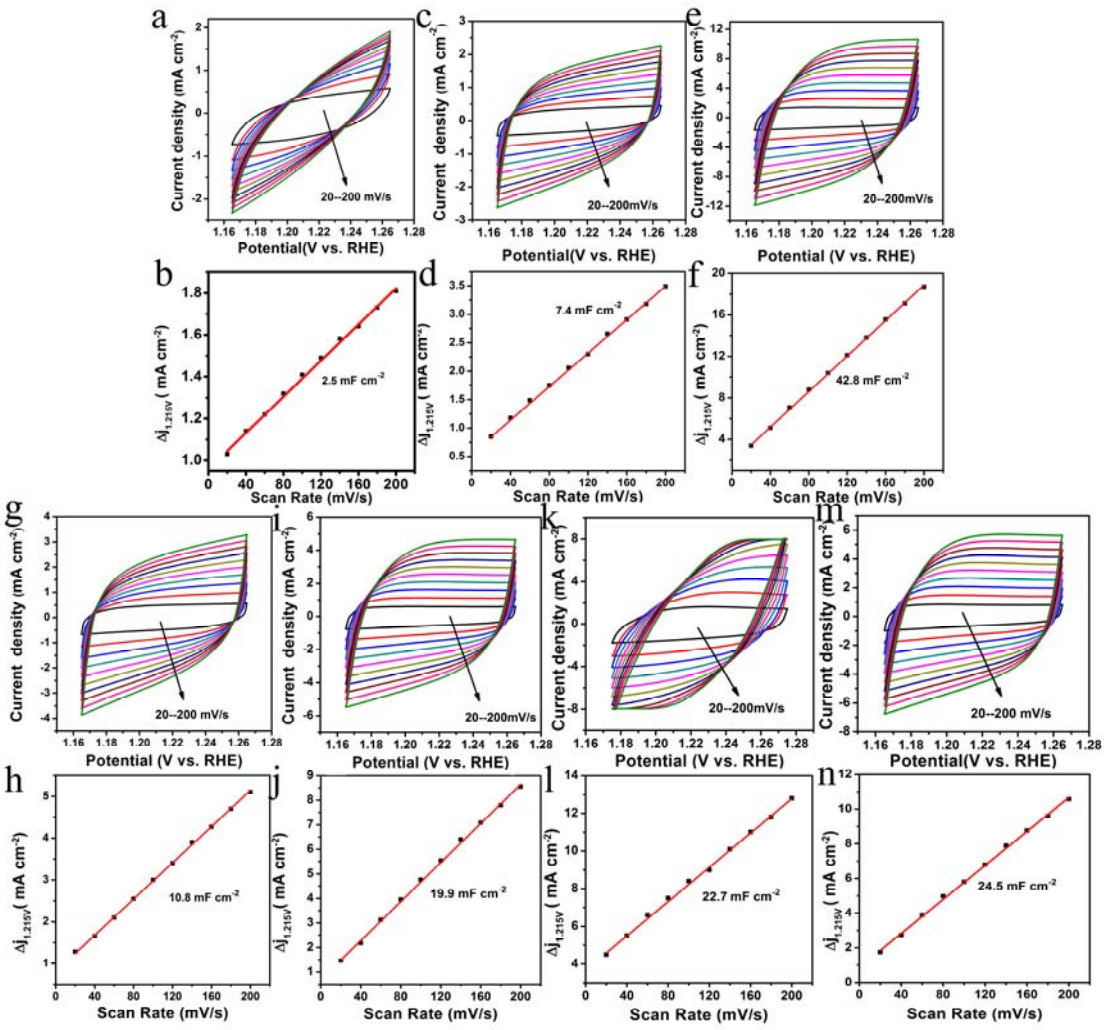

Figure S28. Cyclic voltammograms (CVs) in the region of 1.164 V-1.264 V with the different rates for **(a)** Mo-MOFs-T5; **(c)** ZIF-67-T5; **(e)** S-2-T5; **(g)** S-2-T4; **(i)** S-2-T6; **(k)** S-1-T5; **(m)** S-3-T5 in 1.0 M KOH. The capacitive current at 0.135 V as a function of scan rate for **(b)** Mo-MOFs-T5; **(d)** ZIF-67-T5; **(f)** S-2-T5; **(h)** S-2-T4; **(j)** S-2-T6; **(l)** S-1-T5; **(n)** S-3-T5, respectively ($\Delta j_0 = j_a - j_c$).

In order to directly illustrate that the material has better electrocatalytic oxygen evolution performance. We also performed the electrocatalytic oxygen double-layer capacitance test to give the electrochemically surface area (ECSA) of different materials. The capacitance of S-2-T5 is about 42.8 mF cm^{-2}, much higher than ZIF-67-T5 (7.4 mF cm^{-2}), Mo-MOFs-T5 (2.5 mF cm^{-2}), S-2-T4 (10.8 mF cm^{-2}), S-2-T6 (19.9 mF cm^{-2}), S-1-T5 (22.7 mF cm^{-2}) and S-3-T5 (24.5 mF cm^{-2}).

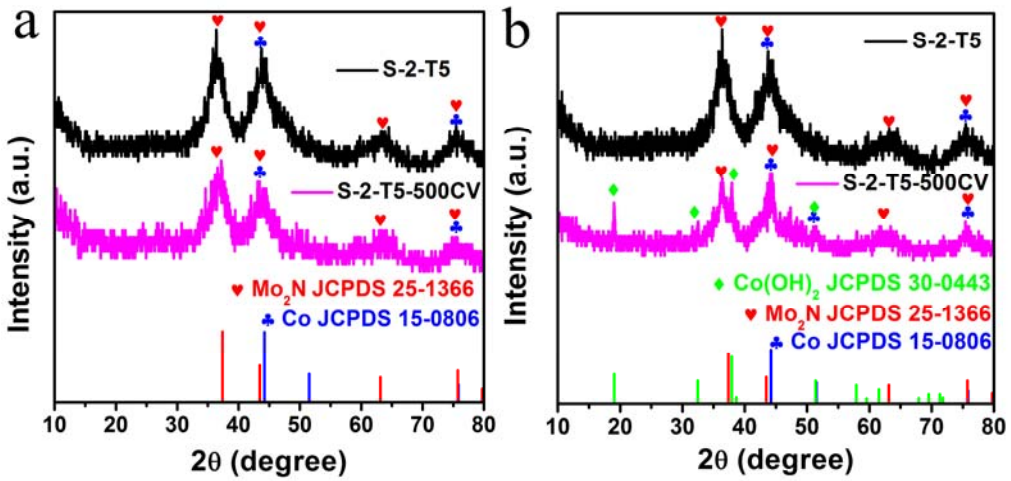

Figure S29. (a) XRD pattern of S-2-T5 after HER test (500 CV cycles). (b)XRD pattern of S-2-T5 after OER test (500 CV cycles).

Figure S29a shows XRD pattern of S-2-T5 after HER test (500 CV cycles). It is shown that the catalysts have no obvious change after HER test. Figure S29b shows XRD pattern of S-2-T5 after OER test (500CV). In addition to the characteristic peaks of molybdenum nitride and cobalt, a characteristic peak of $Co(OH)_2$ is also present in the material S-2-T5-500CV. The XRD diffraction peaks are consistent at 2θ= 19.06°, 32.47°, 37.92° and 51.36° can be indexed to the (001), (100), (101) and (102) facets of $Co(OH)_2$ (JCPDS 30-0443).

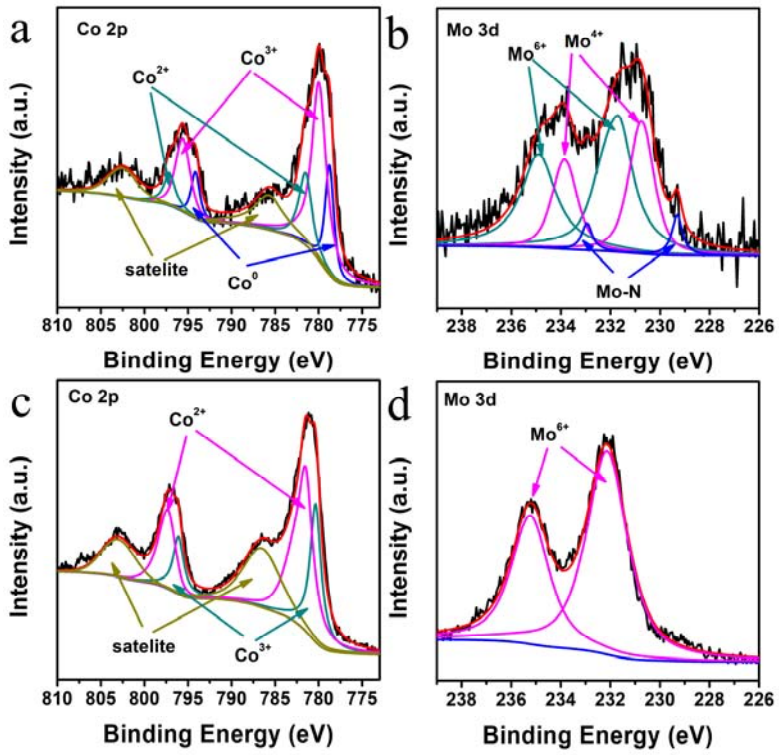

Figure S30. The XPS of (a) Co 2p and (b) Mo 3d of S-2-T5 after HER test (500 CV cycles); (c) Co 2p and (d) Mo 3d of S-2-T5 after OER test (500 CV cycles).

Figure S30a shows high-resolution XPS spectrum of Co element of S-2-T5 after HER test, which is similar to that of original S-2-T5. Specifically, the spin-orbit splitting is approximately 15.8 eV, which indicates the co-existence of Co (II) and Co (III). The peaks at about 781.2 eV and 797.1 eV correspond to Co $2p_{3/2}$ and Co $2p_{1/2}$ of Co^{2+}, respectively, which are accompanied by a couple of satellite peaks located at 785.7 eV and 802.5 eV. The BE at about 779.9 eV and 795.6 eV are attributed to Co $2p_{3/2}$ and Co $2p_{1/2}$ of Co^{3+}. The peaks located at 778.7 eV and 794.1 eV in Co 2p spectrum represent Co^0 $2p_{3/2}$ and Co^0 $2p_{1/2}$, respectively. The results indicate good stability of Co in HER test. For Mo XPS, we can observe the decrease of N-Mo peak and increase of Mo^{4+} and Mo^{6+} peaks (Figure S30b). The peaks at the binding energies (BE) of 229.3 eV and 233.0 eV are classified as Mo $3d_{5/2}$ and Mo $3d_{3/2}$ of Mo^{4+}. The peaks at BE of 231.7 eV and 234.9 eV are attributed to Mo $3d_{5/2}$ and Mo $3d_{3/2}$ of Mo^{6+}. The binding peaks at 229.3 eV and 232.9 eV are defined as the BE of the Mo-N bond. The change should be ascribed to the formation of hydroxyl on Mo_2N in KOH solution. Similar phenomenon have been observed for NiCoP.[21]

The high resolution XPS spectra of the Co element of S-2-T5 after OER test

shows that the Co 2p spectra can be fitted into six peaks (Figure S30c). The two peaks at 780.4 and 796.1 eV corresponding to the $2p_{3/2}$ and $2p_{5/2}$ of Co^{3+}. The peaks related to Co^{2+} $2p_{3/2}$ and $2p_{5/2}$ are located at 781.5 and 797.3 eV, which are accompanied by a couple of satellite peaks located at 786.3 eV and 803.0 eV. The XPS of Co^{2+} and Co^{3+} can be ascribed to $Co(OH)_2$, being consistent with XRD result. High resolution XPS spectra of Mo elements of S-2-T5 after OER test are shown in Figure S30d. The Mo 3d spectra can be fitted into two peaks. The peaks at the binding energies of 232.1 eV and 235.2 eV are attributed to Mo $3d_{5/2}$ and Mo $3d_{3/2}$ of Mo^{6+}. The Mo_2N is oxidized to the high-valence Mo species (Mo^{6+}) during OER process in alkaline solution. The presence of high-valence species is also favorable to improve the activity of catalyst. The results are also observed in previous reports.[9,24]

Table S1. The naming and experimental parameters of samples

Sample	Feed ratio of Mo-MOFs to Co	calcination temperature (^{0}C)	Samples name
Mo-MOFs	/	500	Mo-MOFs-T5
ZIF-67	/	500	ZIF-67-T5
ZIF-67/Mo-MOFs-2	2:20	400	S-2-T4
	2:20	500	S-2-T5
	2:20	600	S-2-T6
ZIF-67/Mo-MOFs-1	1:20	500	S-1-T5
ZIF-67/Mo-MOFs-3	3:20	500	S-3-T5

Table S2. Elements and content in ZIF-67/Mo-MOFs-2, S-2-T5, Mo-MOFs-T5 and ZIF-67-T5 samples tested by XPS.

Sample	Atomic Conc %				
	Co 2p	O 1s	N 1s	C 1s	Mo 3d
ZIF-67/Mo-MOFs-2	3.60	11.27	17.46	65.11	2.56
ZIF-67-T5	5.28	6.89	8.58	79.25	0.00
Mo-MOFs-T5	0.00	16.91	40.98	31.64	10.47
S-2-T5	15.15	24.23	11.40	46.13	2.80

Table S3. Elements and content in ZIF-67/Mo-MOFs-2, S-2-T5, Mo-MOFs-T5 and ZIF-67-T5 samples tested by XPS.

Sample	Mass Conc %				
	Co 2p	O 1s	N 1s	C 1s	Mo 3d
ZIF-67/Mo-MOFs-2	12.74	10.83	14.69	45.97	14.76
ZIF-67-T5	20.85	7.38	8.04	63.73	0.00
Mo-MOFs-T5	0.00	12.14	25.75	17.05	45.06
S-2-T5	39.38	17.31	7.04	24.44	11.84

Table S4. BET surface areas of the prepared samples.

Sample	Surface Area ($m^2 g^{-1}$)
Mo-MOFs	6
ZIF-67	1512
ZIF-67/Mo-MOFs-2	1143
Mo-MOFs-T5	57
ZIF-67-T5	6
S-2-T5	9

Table S5. The summary of the catalytic performance of various catalysts for HER.

Samples	η_0 (mV)	η_{10} (mV)	η_{20} (mV)	η_{50} (mV)	η_{100} (mV)	Tafel slope (mV dec^{-1})	j_0 ($mAcm^{-2}$)
S-2-T5	**23**	**76**	**106**	**167**	**240**	**47**	**0.302**
Mo-MOFs-T5	155	296	344	427	517	61	0.025
ZIF-67-T5	72	180	221	295	377	87	0.019
Pt/C	2	32	48	92	158	31	/
S-1-T5	48	93	129	200	280	66	/
S-3-T5	39	87	121	186	261	61	/
S-2-T4	32	106	144	215	293	58	/
S-2-T6	38	110	152	232	320	59	/

Table S6. The summary of the catalytic performance of various catalysts for OER.

Samples	η_{10} (mV)	η_{20} (mV)	η_{50} (mV)	η_{100} (mV)	Tafel slope (mV dec^{-1})
S-2-T5	**302**	**334**	**400**	**485**	**90**
Mo-MOFs-T5	407	442	509	604	93
ZIF-67-T5	387	422	488	581	92
RuO_2	355	389	456	546	104
S-1-T5	356	387	453	541	97
S-3-T5	333	365	430	522	101
S-2-T4	348	378	439	525	102
S-2-T6	312	346	441	514	96

Table S7. The summary of the catalytic performance of various catalysts for overall water splitting.

Samples	η_{10}(V)	η_{20}(V)	η_{50} (V)
Co-Mo_2N||Co-Mo_2N	**1.576**	**1.671**	**1.832**
Pt/C||RuO_2	1.630	1.701	1.855

Table S8. The summary of the performance of different catalysts for HER.

Catalyst	Tafel slope ($mVdec^{-1}$)	η_{10} (mV)	Electrolyte	References
S-2-T5	**47**	**23**	**1 M KOH**	**This work**
MoN-NC	54	42	0.5M H_2SO_4	1
MoC_x	59	151	1 M KOH	2
MoO_2@PC-RGO	41	64	0.5M H_2SO_4	3
Mo_2C@NPC/NPRGO	33.6	34	0.5M H_2SO_4	4
Co-Mo_2C	39	38	0.5M H_2SO_4	5
Mo_2N/NC	115.7	151	0.5M H_2SO_4	6
Mo_2N- Mo_2S	59	190	0.5M H_2SO_4	7
MoP/rGO	72	140	1 M KOH	8
MoP/rGO	58	119	0.5M H_2SO_4	8
WN- Mo_2N/CNTs	115	315	0.5M H_2SO_4	9
HF-MoSP	85	119	1 M KOH	10
HF-MoSP	29	108	0.5M H_2SO_4	10
Fe_3C/ Mo_2C @NPGC	45.2	150	0.5M H_2SO_4	11
MoC_x@C	56	79	0.5M H_2SO_4	12
MoP@PC	66	153	0.5M H_2SO_4	13
$MoNi_4$/ MoO_{3-x}	36	17	1 M KOH	14
Co-N- MoO_2	126.8	258	0.1 M KOH	15
Ni_3N-NiMoN-5	64	31	1 M KOH	22
Ni_2P/Ni/NF	72	98	1 M KOH	23
$NiCo_2O_4$ (iR compensation)	49.7	50	1 M KOH	24
MoO_2/Ni foam	41	25	1 M KOH	25
Co-P/NC-based	51	191	1 M KOH	26
MoS_2/Ni_3S_2	81	110	1 M KOH	27
Ni_5P_4	40	140	1 M KOH	28
Ni_5P_4	53	150	0.5 M H_2SO_4	28
NiMoN-550	79	89	1 M KOH	30
NC@$CuCo_2N_x$/CF	76	105	1 M KOH	31
$NiMoP_2$	56	195	0.5 M H_2SO_4	32

Table S9. The summary of the performance of different catalysts for OER.

Catalyst	Tafel slope ($mVdec^{-1}$)	η_{10} (mV)	Electrolyte	References
S-2-T5	**90**	**302**	**1 M KOH**	**This work**
NiCo-POM/Ni	126	360	0.1 M KOH	16
CoO_x-MoC/NC-2	89.8	330	1 M KOH	17
CoNC@MoS_2/CNF films	51.9	350	1 M KOH	18
Co-P/NC-based	52	354	1 M KOH	19
Co_9S_8@MoS_2/CNFs	61	430	1 M KOH	20
NiMo HNRs/TiM	47	310	1 M KOH	21
Ni_3N-NiMoN-5	118	277	1 M KOH	22
Ni_2P/Ni/NF	/	200	1 M KOH	23
$NiCo_2O_4$ (iR compensation)	53	1.52	1 M NaOH	24
MoO_2/Ni foam	54	1.49	1 M KOH	25
Co-P/NC-based	52	354	1 M KOH	26
MoS_2/Ni_3S_2	88	218	1 M KOH	27
Ni_5P_4	/	218	1 M KOH	28
Ni-P foam	23/179.9	100	1 M KOH	29
NiMoN-550	η_{10}=295	94	1 M KOH	30
NC@$CuCo_2N_x$/CF	η_{10}=230	84	1 M KOH	31
$NiMoP_2$	η_{20}=260	90.6	1 M KOH	32

Table S10. The summary of the performance of different catalysts for overall water splitting in alkaline electrolytes.

Catalyst	Overall voltage at 10 $mAcm^{-2}$(V)	Electrolyte	References
S-2-T5	**1.576**	**1 M KOH**	**This work**
CoNC@MoS_2/CNF films	1.62	1 M KOH	18
NiMo HNRs/TiM	1.64	1 M KOH	21
Ni_3N-NiMoN-5	1.54	1 M KOH	22
Ni_2P/Ni/NF	1.49	1 M KOH	23
$NiCo_2O_4$	1.65	1 M NaOH	24
MoO_2/Ni foam	1.53	1 M KOH	25
Co-P/NC-based	η_{165}=2	1 M KOH	26
MoS_2/Ni_3S_2	1.56	1 M KOH	27
Ni_5P_4	1.7	1 M KOH	28
Ni-P foam	η_5=1.44	1 M KOH	29
NiMoN-550	1.596	1 M KOH	30
NC@$CuCo_2N_x$/CF	1.62	1 M KOH	31
$NiMoP_2$	1.65	1 M KOH	32

References

1 Y. P. Zhu, G. Chen, X. M. Xu, G. M. Yang, M. L. Liu and Z. P. Shao, *ACS Catal.*, 2017, **7**, 3540-3547.

2 H. B. Wu, B. Y. Xia, L. Yu, X.-Y, Yu and X. W. Lou, *Nature Communications*, 2015, **6**, 6512.

3 Y.-J. Tang, M.-R. Gao, C.-H. Liu, S.-L. Li, H.-L. Jiang, Y.-Q. Lan, M. Han and S.-H. Yu, *Angew. Chem. Int. Ed.*, 2015, **54**, 12928-12932.

4 J.-S. Li, Y. W, C.-H. Liu, S.-L. Li, Y.-G. Wang, L.-Z. Dong, Z.-H. Dai, Y.-F. Li and Y.-Q. Lan, *Nat Commun.*, 2016, **7**, 11204.

5 H. L. Lin, N. Liu, Z. P. Shi , Y. L. Guo, Y. Tang and Q. S. Gao, *Adv. Funct. Mater.*, 2016, **26**, 5590-5598.

6 Y.-J. Song and Z.-Y. Yuan, *Electrochimica Acta*, 2017, **246**, 536-543.

7 K. Ojha, S. Saha, S. Banerjee and A. K. Ganguli, *ACS Appl. Mater. Interfaces.*, 2017, **9**, 19455-19461.

8 H. J. Yan, Y. Q. Jiao, A. P. Wu, C. G. Tian, X. M. Zhang, L. Wang, Z. Y. Ren and H. G. Fu, *ChemComm*., 2016, **52**, 9530-9533.

9 M. C. Meng, H. J. Yan, Y. Q. Jiao, A. P. Wu, X. M. Zhang, R. H. Wang and C. G. Tian, *RSC Adv*., 2016, **6**, 29303-29307.

10 A. P. Wu, C. G. Tian, H. J. Yan, Y. Q. Jiao, Q. Yan, G. Y. Yang and H. G. Fu, *Nanoscale*, 2016, **8**, 11052-11059.

11 J.-S. Li, Y.-J. Tang, C.-H. Liu, S.-L. Li, R.-H. Li, L.-Z. Dong, Z.-H. Dai, J.-C. Bao and Y.-Q. Lan, *J. Mater. Chem. A.*, 2016, **4**, 1202-1207.

12 X. J. Yang, X. J. Feng, H. Q. Tan, H. Y. Zang, X. L. Wang, Y. H. Wang, E. Wang and Y. G. Li, *J. Mater. Chem. A.*, 2016, **4**, 3947-3954.

13 J. Yang, F. J. Zhang, X. Wang, D. S. He, G. Wu, Q. H. Yang, X. Hong, Y. Wu and Y. D. Li, *Angewandte Chemie*, 2016, **128**, 13046-13050.

14 Y-Y. Chen, Y. Zhang, X. Zhang, T. Tang, H. Luo, S. A. Niu, Z.-H. Dai, L-J. Wan and J.-S. Hu, *Advanced Materials*, 2017, **29**, 1703311.

15 L. J. Yang, J. Y. Yu, Z. Q. Wei, G. X. Li, L. D. Cao, W. J. Zhou and S. W. Chen, *Nano Energy*, 2017,**41**, 772-779.

16 W. J. Luo, J. Hu, H. L. Diao, B. Schwarz, C. Streb and Y.-F. Song, *Angewandte Chemie-International Edition*, 2017, **56**, 4941-4944.

17 T. Huang, Y. Chen and J-M. Lee, *Small*, 2017, **13**, 1702753.

18 D. X. Ji, S. J. Peng, L. Fan, L. L. Li, X. H. Qin and S. Ramakrishna, *Journal of Materials Chemistry A*, 2017, **5**, 23898-23908.

19 B. You, N. Jiang, M. L. Sheng, S. Gul, J. Yano and Y. J. Sun, *Chemistry of materials*, 2015, **27**, 7636-7642.

20 H. Zhu, J. F. Zhang, R. P. Y-Z, M. L. Du, Q. F. Wang, G. H. Gao, J. D. Wu, G. M. Wu, M. Zhang, B. Liu, J. M. Yao and X. W. Zhang, *Advanced materials*, 2015, **27**, 4752–4759.

21 J. Q. Tian, N. Y. Cheng, Q. Liu, X. P. Sun, Y. Q. He and A. M. Asiri, *Journal of Materials Chemistry A*, 2015, **3**, 20056-20059.

22 A. P. Wu, Y. Xie, H. Ma, C. G. Tian, Y. Gu, H. J. Yan, X. M. Zhang, G. Y. Yang and H. G. Fu, *Nano Energy*, 2018, **44**, 353-363.

23 B. You, N. Jiang, M. L. Sheng, M. W. Bhushan and Y. J. Sun, *ACS Catalysis*, 2016, **6**, 714-721.

24 X. H. Gao, H. X. Zhang, Q. G. Li, X. G. Yu, Z. L. Hong, X. W. Zhang, C. D. Liang and Z. Lin, *Angewandte Chemie International Edition*, 2016, **55**, 6290-6294.

25 Y. S. Jin, H. T. Wang, J. J. Li, X. Yue, Y. J. Han, P. K. Shen and Y. Cui, *Advanced Materials*, 2016, **28**, 3785-3790.

26 B. You, N. Jiang, M. L. Sheng, S. Gul, J. Yano and Y. J. Sun, *Chemistry of materials*, 2015, **27**, 7636-7642.

27 J. Zhang, T. Wang, D. Pohl, B. Rellinghaus, R. H. Dong, S. H. Liu, X. D. Zhuang and X. L. Feng, *Angewandte Chemie-International Edition*, 2016, **128**, 6814-6819.

28 M. Ledendecker, S. K. Calderyn, C. Papp, H.-P. Steinruck, M. Antonietti and M. Shalom, *Angewandte Chemie-International Edition*, 2015, **127**, 12538-12542.

29 X. G. Wang, W. Li, D. H. Xiong and L. F. Liu, *Journal of Materials Chemistry A*, 2016, **4**, 5639-5646.

30 Z. X. Yin, Y. Sun, C. L. Zhu, C. Y. Li, X. T. Zhang and Y. J. Chen, *Journal of Materials Cheistry A*, 2017, **5**, 13648-13658.

31 J. Zheng, X. L. Chen, X. Zhong, S. Q. Li, T. Z. Liu, G. L. Zhuang, X. N. Li, S. W. Deng, D. H. Mei and J-G. Wang, *Adv. Funct. Mater*., 2017, **27**, 1704169.

32 X.-D. Wang, H.-Y. Chen, Y.-F. Xu, J.-F. Liao, B.-X. Chen, H.-S. Rao, D.-B. Kuang and C.-Y. Su, *Journal of Materials Chemistry A*, 2017, **5**, 7191-7199.